# UC San Diego
## UC San Diego Previously Published Works

**Title**

In situ crack mapping of large-scale self-sensing concrete pavements using electrical resistance tomography

**Permalink**

https://escholarship.org/uc/item/1nb224vq

**Authors**

Gupta, Sumit
Lin, Yun-An
Lee, Han-Joo
et al.

**Publication Date**

2021-09-01

**DOI**

10.1016/j.cemconcomp.2021.104154

Peer reviewed

# In Situ Crack Mapping of Large-Scale Self-Sensing Concrete Pavements using Electrical Resistance Tomography

Sumit Gupta[1], Yun-An Lin[1], Han-Joo Lee[2], Jeff Buscheck[3], Rongzong Wu[3], Jerome P. Lynch[4], Navneet Garg[5], and Kenneth J. Loh[1,2,*]

[1]Department of Structural Engineering, University of California San Diego, La Jolla, CA, 92093, USA
[2]Materials Science and Engineering Program, University of California San Diego, La Jolla, CA, 92093, USA
[3]Department of Civil and Environmental Engineering, University of California Davis, Davis, CA 95616, USA
[4]Department of Civil and Environmental Engineering, University of Michigan, Ann Arbor, MI 48109, USA
[5]William J. Hughes Technical Center, Federal Aviation Administration, Atlantic City, NJ 08405, USA
*Corresponding author e-mail: kenloh@ucsd.edu

## Abstract

This study aims to validate the large-scale application of self-sensing concrete in airport runway pavements and to use electrical resistance tomography (ERT) for characterizing spatially distributed damage during accelerated pavement testing. This self-sensing concrete not only retains the expected mechanical properties of typical airport pavements, but it can also sense deformation and strain. First, sensing properties were encoded in concrete pavements by modifying the cement-aggregate interface with multi-walled carbon nanotube (MWCNT) thin films. MWCNT thin films were spray-coated onto dried fine and coarse aggregates, and the film-coated aggregates were directly used for concrete casting. Second, an ERT algorithm was implemented for spatial conductivity mapping of self-sensing concrete pavements. Extensive laboratory tests were conducted on different sized specimens for characterizing their spatial damage detection performance. Last, a full-scale concrete airport pavement slab was cast with self-sensing concrete patches at locations where damage was expected. A heavy vehicle simulator was employed for accelerated pavement testing to induce cracks, while ERT measurements were collected at periodic intervals during testing. The results confirmed that the severities, locations, and patterns of cracks could be identified from the reconstructed ERT conductivity maps. Furthermore, subsurface damage features were identified prior to these cracks propagated and became visible on the surface.

**Keywords:** Accelerated pavement testing, conductivity, cracks, carbon nanotube, concrete, damage detection, EIT, ERT, nanocomposite, structural health monitoring

## 1. Introduction

Airport pavements are designed and constructed to withstand severe loads imposed by aircraft. To meet these requirements, rigid airport pavements are generally made of discrete concrete slabs connected by longitudinal and transverse joints and dowels [4]. The increase in weight and size of aircrafts over the last few decades to meet the rising demands of air transport have imposed greater load demands on airport pavements. Studies on airfield traffic have revealed that many aircraft with these higher weight and new landing gear configurations cause damage to airport pavements [5], which poses a safety hazard and is a major source of delays. Severe pavement damage can even disrupt or shutdown aircraft takeoff and landing operations, resulting in substantial economic losses due to flight cancellations, detours, or even damage to aircraft landing gears. For example, a Raytheon Premier One jet suffered damage to its landing gear after running over a blowup failure on the runway at Ankeny Regional Airport in Iowa [6]. Therefore, to ensure safe and efficient flight operations, condition assessment of airport pavements needs to be performed in a regular and timely fashion.

Most of the airport pavement monitoring techniques today rely on visual inspection. Although visual inspection can detect damage such as surface cracks, blowups, and undulations, among others, they are time-, labor-, and cost-intensive [7]. The inability to shut down an airport for extended periods means that inspectors may not have sufficient time to perform a thorough investigation. In addition, damage often initiates subsurface, making them difficult to detect by visual inspection.

Computer vision-based pavement monitoring methods have superseded visual inspection as an easy-to-deploy and low-cost monitoring strategy with higher accuracy than visual inspection [8]. Images and videos of the pavement surfaces taken by high-speed cameras are processed through image processing algorithms for detecting anomalies and cracks [9, 10]. However, the robust detection of cracks can be challenging due to nonuniform surface textures, background complexity, and the presence of non-crack features (*e.g*., structural boundaries, wires, corrosion marks, or joints) [9, 11]. Furthermore, advanced optical cameras with night vision capabilities are needed if continuous monitoring (24 h) is desired. Nonetheless, subsurface cracks that have not propagated to the pavement's surface cannot be detected using vision-based methods.

Thus, an alternative is to rely on embedded sensors, such as foil-based strain gages, in pavements for achieving more accurate and reliable condition assessment. For instance, Zhao *et al*. [12] embedded strain gages for monitoring the performance of a new runway pavement at Shanghai Airport in China. Strain gages were also installed in the Newark International Airport (EWR), New Jersey, airport runway to detect delamination in asphalt overlay [13]. Henschen *et al*. [14] used dynamic strain gages to investigate the relative effectiveness of various isolation joint arrangements in concrete pavements at the Chicago O'Hare airport in Illinois. However, strain gages only measure localized strains in the immediate vicinity where they are installed, which may not coincide with the location of cracks or damage. Therefore, densely distributed strain monitoring using an array of strain gages is often needed to infer the likelihood of pavement damage, but such instrumentation plans require a large number of sensing channels and increases operating and maintenance costs. Another approach of distributed strain monitoring is to leverage fiber Bragg grating (FBG) sensors and to embed them in concrete during casting [15]. FBG sensors and fiber optic cables are lightweight, compact, corrosion-resistant, highly sensitive, and immune to electromagnetic interference. However, FBG measurements are susceptible to temperature [16]. Their high installation cost has also restricted their widespread use in airport pavement condition assessment applications [17].

Advanced nondestructive evaluation (NDE) techniques, such as ground-penetrating radar (GPR) and spectral analysis of surface waves (SASW), have been used for pavement monitoring [18]. Unfortunately, they also suffer from high costs, low measurement accuracy, and complexity of data processing. Infrared thermography has been demonstrated for assessing near-surface damage in pavements [19]. However, thermography is sensitive to ambient conditions, emissivity values, and surface temperature variations of the pavement [20], not to mention that they are limited to near-surface applications. Moreover, a major limitation of these aforementioned NDE methods is that they can only be performed manually when that section of the airport is shutdown.

Instead of treating sensing and health monitoring as an afterthought, multifunctional concrete pavements that could bear loads while sensing features indicative of damage have been proposed. The most widely used design approach is to disperse and embed conductive fillers (*e.g*., carbon black [21], carbon nanotube (CNT) [22], nickel powder [23], and graphite [24], to name a few) in the cement matrix during concrete casting. In particular, nanomaterials such as CNTs have been widely studied due to their excellent physical [25] and electromechanical properties [26], which are promising for improving the mechanical and sensing properties of cement composites. For example, Li *et al*. [27] and Yu and Kwon [28] treated multi-walled carbon nanotubes (MWCNT) with an acid mixture to fabricate piezoresistive cementitious composites. Han *et al*. [29] showed that MWCNT cement composites can be used for traffic monitoring. Despite successfully demonstrating strain and damage monitoring, these casting procedures require dispersing large quantities of conductive fillers, which is expensive [29, 30], modifies cement paste

Table 1. Previous results of self-sensing concrete with spray-coated MWCNT-latex thin film interfaces

| References | Major findings | Findings used in this study |
|---|---|---|
| Loh and Gonzalez [1] (2015) | • Electrical properties of mortar casted with spray-coated sand exhibited extremely high bilinear strain sensitivities <br> – Gage factor ~ 224 (below -0.2% strain) <br> – Gage factor ~ 60 (above -0.2% strain) <br> • Consistent electrical response over multiple cycles of loading | The method of pre-coating aggregates with nanocomposite coatings was adopted. |
| Gonzalez *et al.* [2] (2016) | • MWCNT-latex films affected the stiffness and strength of mortar specimens <br> • ERT was able to identify the location, shape, size, and severity of spatially distributed damage in self-sensing mortar specimens | The ERT forward problem was used. |
| Gupta *et al.* [3] (2017) | • Mechanical properties (compressive and flexural strength) of the self-sensing concrete, fabricated by modifying the cement-aggregate interfaces with MWCNT-latex thin films, could be maintained or, in certain cases, even exceeded that of untreated concrete <br> • Spatial damage detection: <br> – ERT successfully characterized damage induced in (1) sand-coated and (2) both sand- and aggregate-coated self-sensing concrete <br> – ERT was unable to detect spatially distributed damage in (3) untreated concrete and (4) large aggregate-coated specimens <br> • ~ 90% cost reduction as compared to the direct dispersion of MWCNTs in cement matrix | The concrete mix design and established self-sensing concrete casting procedures were adapted for casting at scale. |

rheology [31], changes existing casting procedures [32], and is difficult to scale-up [33]. Furthermore, nanomaterial dispersion in cement pastes remains challenging, and nonuniform nanomaterial distributions can degrade the bulk cement composite's mechanical and electrical properties.

As opposed to dispersing nanomaterials in the cement matrix, previous studies [1-3, 34, 35] explored the modification of the cement-aggregate interface using MWCNT-based thin films. Here, an MWCNT-based ink was deposited onto the surfaces of dried fine and coarse aggregates prior to casting. Then, the film-coated aggregates were directly used for casting concrete. It was found that this procedure yielded concrete specimens that had sufficient electrical conductivity and strain-sensitive electromechanical properties [1]. This design method did not affect cement paste rheology nor did it change existing concrete casting procedures. Since the electrical conductivity at every location in the cement composite was sensitive to strain and damage, an electrical resistance tomography (ERT) measurement strategy and algorithm was implemented for mapping their conductivity distribution and for localizing damage features [2, 3]. Laboratory tests on small-scale specimens showed that the severities and locations of artificially introduced damage could be correctly identified. The issue of cost was also addressed, since orders of magnitude lower concentrations of MWCNTs were used than directly dispersing them in the cement paste [3]. The major findings from these previous studies are summarized in Table 1. What is missing is the demonstration and performance characterization of these materials at large-scale and in more realistic operations conditions, which is crucial before the technology can be translated to industry practice.

Therefore, the objective of this study was to validate spatial damage monitoring during accelerated pavement testing of a full-scale concrete airport pavement with self-sensing concrete regions. A $15\times12$ ft$^2$ ($4.6\times3.7$ m$^2$) concrete pavement was cast with four $18\times12$ in$^2$ ($0.46\times0.30$ m$^2$) smart concrete regions. The

self-sensing concrete mix design was informed by previous studies [2, 3] to maximize ERT damage sensitivity and signal-to-noise ratio (SNR). A heavy vehicle simulator (HVS) applied repeated aircraft wheel loads on the pavement, while ERT conductivity distributions were obtained at periodic intervals for damage monitoring. This article begins with a brief discussion of ERT and its mathematical formulation. Then, the procedure for preparing the film-coated aggregates, as well as the concrete mix design and casting procedures, are presented. Finally, small-scale laboratory tests and the full-scale accelerated pavement test procedures and results are discussed. The article ends with a brief conclusion of major findings.

## 2. ERT Background

Electrical impedance tomography (EIT) or ERT is a soft-field imaging technique that uses a set of boundary electrical measurements to estimate the distribution of electrical conductivity of a predefined sensing region [36]. Since its discovery, EIT has been successfully used in healthcare, such as for brain imaging in newborns and adults [37], respiratory system monitoring [38], gastric acid secretion monitoring [39], and myoskeletal imaging [40]. More recently, multifunctional nanocomposites coupled with EIT have been demonstrated for structural health monitoring (SHM). Some of its earliest works include using EIT with nanocomposite thin films for distributed monitoring of strain and pH [41] and subsurface impact damage in glass fiber-reinforced polymer composites [42].

Since then, EIT has found applications for SHM of cement composite components and structures. Hou and Lynch [43] used EIT for visualizing distributed flexural micro-cracks that developed during three-point bending of engineered cementitious composite beam specimens. Hallaji *et al*. [44] deposited a thin electrically conductive copper paint onto the surface of a concrete beam. During three-point bending testing, the rupture of both the concrete and coated copper paint caused a decrease in the paint's electrical conductivity, which was correctly estimated by EIT. Seppanen *et al*. [45] proposed a multi-layered, multifunctional coating consisting of electrically insulated colloidal copper and silver paint layers for corrosion and crack sensing. Laboratory experiments have demonstrated that the copper paint layer was sensitive to cracking and corrosion, while the silver paint layer was sensitive to only cracking. Tallman *et al*. [46] showed that the conductivity distribution of a carbon nanofiber specimen changed due to the application of loads. They were able to use the EIT-estimated change in conductivity distribution as an input to an inverse piezoresistive model to assess the deformation and strain pattern of the specimen.

Besides direct damage monitoring, absolute and difference EIT imaging algorithms were investigated for characterizing transport in cementitious composites [47]. Hallaji *et al*. [48] found that EIT was able to identify moisture propagation, along with an approximate shape and position of the waterfront in concrete specimens. Suryanto *et al*. [49] demonstrated the ability of a difference imaging technique for monitoring water movement within concrete. However, difference imaging was suitable for qualitative unsaturated flow monitoring at the early stage of ingress. Later, Smyl *et al*. [50] implemented a linearized absolute reconstruction algorithm for quantitative assessment of concrete's volumetric moisture content. Given the limitation of point-based moisture monitoring techniques [51], EIT's ability to resolve the spatial-temporal state and distribution of moisture in concrete has paved a new path for understanding its durability. Despite these advancements, large-scale *in situ* applications of EIT for spatially distributed damage detection in concrete structures have not been studied.

In order to use EIT, the target conductive body ($\Omega$) is instrumented with a set of equidistantly spaced boundary electrodes. Low magnitude alternating current (AC) is injected between a pair of boundary electrodes, while the induced voltage differences between other remaining pairs of electrodes are measured. Each unique boundary electrode pair is then excited in a predefined sequence, and the corresponding voltage and phase measurements are recorded to obtain the full set of boundary voltage responses. The measured set of voltage responses are then used to solve the EIT inverse problem and to reconstruct the spatial impedance distribution of $\Omega$. Previous studies showed that MWCNT thin film's resistance is sensitive to applied strains [1]. Since resistance of piezoresistive materials are directly correlated to its conductivity, this study utilized a low-magnitude direct current (DC) for interrogating self-sensing concrete specimens.

Because DC was used, this meant that electrical resistance tomography was conducted to reconstruct their spatial conductivity distributions (*i.e.*, the real part of the complex-valued impedance) [2, 48].

In general, the EIT or ERT algorithm consists of two parts, which are the forward and inverse problems, and will be briefly summarized in the next subsections. More detailed descriptions of the EIT method are discussed in previous studies [2, 3].

### 2.1. Forward Problem

The forward problem is solved to estimate the boundary voltage responses when the conductivity distribution ($\sigma$) and the current injection patterns are known *a priori*. Mathematically, the EIT or ERT forward problem can be described by the 2D Laplace's equation:

$$\nabla \cdot (\sigma \nabla u) = 0 \tag{1}$$

where $u$ is the electric potential distribution over $\Omega$. This second-order partial differential equation is often solved using a finite element (FE) model. The complete electrode model [52] is adopted to define the boundary conditions. In this study, bilinear quadrilateral elements were used to discretize $\Omega$.

### 2.2. Inverse Problem

In practical implementations, the conductivity distribution of a target is desired. The inverse problem estimates the conductivity distribution using experimentally measured boundary voltage sets. In this study, a least-square-based Newton's one-step reconstruction (NOSER) algorithm [52] was used to estimate the conductivity change ($\Delta\sigma$) from the observed change in boundary voltage distribution ($\Delta V$) between two states (*e.g.*, before and after damage) as shown in equation 2.

$$\arg \min_{\Delta\sigma} \|\Delta V - J\Delta\sigma\|^2 \tag{2}$$

where $\Delta V$ is the observed change in boundary voltage distribution between two states, $J$ is the sensitivity matrix (*i.e.*, obtained by the sensitivity method [53]), and $\Delta\sigma$ is the change in electrical conductivity. The NOSER algorithm is a simple and computationally less expensive imaging reconstruction algorithm. In addition, most of the measurement errors can be avoided through difference imaging. However, the EIT or ERT forward problem's nonlinear nature does not allow the cancellation of all modeling errors. Therefore, quantitative assessment of damage cannot be performed using NOSER-reconstructed conductivity maps.

The ill-posed optimization problem described in equation 2 needs to be regularized to obtain a meaningful solution. Regularization was included by appending a penalty term in equation 2:

$$\Delta\sigma = argmin\|\Delta V - J\Delta\sigma\|^2 + \alpha^2\|R(\Delta\sigma - \Delta\sigma_0)\|^2 \tag{3}$$

where $R$, $\alpha$, and $\Delta\sigma_0$ are the regularization matrix, regularization parameter, and some prior assumptions about the conductivity change, respectively. A closed-form solution of $\Delta\sigma$ can be obtained by expanding equation 3 and then setting its derivative to zero, as shown in equation 4.

$$\Delta\sigma = (J^T J + \alpha^2 R^T R)^{-1}(J^T \Delta V - \alpha^2 R^T R \Delta\sigma_0) \tag{4}$$

For the NOSER algorithm, $\Delta\sigma_0$ is set to 0 to obtain the most generalized form of $\Delta\sigma$.

$$\Delta\sigma = (J^T J + \alpha^2 R^T R)^{-1} J^T \Delta V \tag{5}$$

The diagonal of $J^T J$ was used for $R^T R$. More details about the NOSER algorithm can be found in Gupta *et al.* [54]. It should be noted that $\alpha$ needs to be selected on the basis of some prior assumptions about the solution [52]. In this study, the value of $\alpha$ was heuristically set to $10^{-2}$ to achieve meaningful solutions, while an optimum value of $\alpha$ can be obtained using the L-curve method [42, 55].

## 3. Experimental Details

### 3.1. Concrete Mix Design

The concrete mix design used followed Federal Aviation Administration (FAA) guidelines for runway rigid pavements [56], which was also used in a previous study [35]. Sand, coarse aggregates, and cement were used in proportions of 3:2:1, respectively. First, the sand and coarse aggregates were oven-dried at 80 °C for 24 h to eliminate extra moisture. Excess moisture can alter the water-to-cement (w/c) ratio and affect the casted concrete's strength. Second and after drying, the aggregates were cooled to room temperature. These fine and coarse aggregates were then coated with an MWCNT-latex thin film (which will be explained later in Section 3.2). Third, the film-coated coarse aggregates and sand were dried in air and directly used for casting concrete. Last, a w/c ratio of 0.40 was employed. Advacast superplasticizer (SPL) was also added at a concentration of 3.5 mL/kg of cement. The superplasticizer helped reduce the amount of water needed, hence, increasing the strength of concrete while maintaining good workability.

### 3.2. Aggregate Nanocomposite Coating

The MWCNT-based thin films that were deposited onto the aggregates were based on the formulation reported by Mortensen *et al*. [57]. Spray fabrication was used because of its low-cost, efficient, and highly scalable nature. In short, thin film preparation began by dispersing MWCNTs in a 2 *wt.*% aqueous solution of poly(sodium 4-styrenesulfonate) (PSS) via high-energy probe sonication for 1 h. The sonicated MWCNT-PSS solution was mixed with Kynar Aquatec latex and diluted with deionized (DI) water to form the sprayable ink. Next, a Paasche airbrush was used to spray-coat the MWCNT-latex thin film onto the oven-dried sand and coarse aggregates in a fume hood. A shovel was used to mix the aggregates to expose any uncoated aggregates before another layer of film was deposited. For each batch of aggregates, six coatings were deposited on sand and three for the coarse aggregates. The final step entailed oven-drying the film-coated aggregates for 30 min at 80 °C. Although spray-coating was performed manually, the process can be expedited and automated using a robotic spray coater. Furthermore, the aggregates were purposely not fully nor uniformly coated to simulate realistic industry-scale material preparation processes.

### 3.3. Concrete Casting

#### 3.3.1. Small-scale specimens

Plate specimens were cast in customized poly(vinyl chloride) (PVC) molds for laboratory validation of spatial damage detection. Three sample sets of different sizes were made: Type A, $\sim 3.15 \times 3.15 \times 0.7$ in$^3$ ($80 \times 80 \times 18$ mm$^3$) (Fig. 1a); Type B, $\sim 12 \times 12 \times 0.7$ in$^3$ ($300 \times 300 \times 18$ mm$^3$) (Fig. 1b); and Type C, $\sim 20 \times 20 \times 2$ in$^3$ ($500 \times 500 \times 50$ mm$^3$) (Fig. 1c). Type A specimens were instrumented with 24 equidistantly spaced boundary electrodes, while the others used 32 boundary electrodes arranged in $6 \times 6$ and $8 \times 8$ square patterns, respectively. The electrodes were copper mesh strips, which were arranged accordingly on balsa wood formworks to hold them in place during casting (Fig. 1). The length of the electrodes was slightly longer than the specimen's thickness for measurement purposes. Then, the formwork with the electrodes was placed in the PVC mold, while the inner walls of the mold were oiled with WD-40 so that the specimens could be easily removed after casting. The joints of the mold were sealed with white petrolatum.

Casting began by pouring the concrete mix into molds (with the balsa wood formwork and electrodes). Types A and B specimens were cast using only the self-sensing concrete mix. Type C specimens were cast with plain concrete (*i.e*., without coated aggregates) surrounding self-sensing concrete, which simulated the embedment of a self-sensing region within a large pavement section in the field (Fig. 1c). Fabricating these Type C specimens required using an extra temporary mold for containing the inner self-sensing concrete region, which was a 2-mm-thick hollow metal sheet box. After simultaneously pouring the self-sensing concrete mix in the inner region and plain concrete around it, the inner mold was removed after $\sim 5$ min after pouring; doing so allowed both types of concrete to mix at the interface. For all the sample sets, the specimens were wrapped with plastic (to minimize water evaporation and microcracks) and kept in the lab
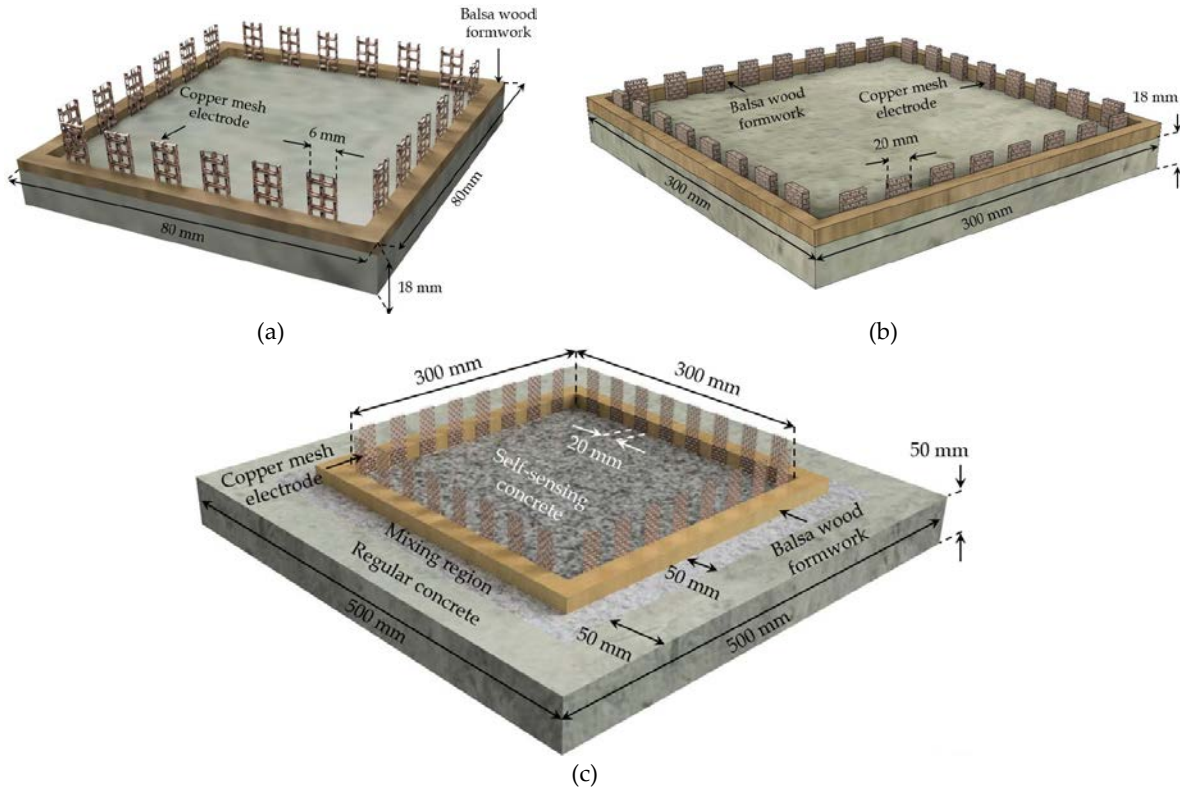
Figure 1. Concrete specimens of different sizes were cast for validating spatial damage detection in the laboratory. Schematics of self-sensing concrete specimens of sizes (a) 80×80×18 mm³ with 24 boundary electrodes (Type A) and (b) 300×300×18 mm³ with 32 boundary electrodes (Type B) are shown. (c) A 500×500×50 mm³ concrete specimen with a 300×300 mm² sensing area at the center was also cast to simulate embedding self-sensing concrete regions in plain concrete.

for 24 h, followed by demolding the specimens and putting them into a curing tank. Smaller specimens were cured for 14 days, and larger specimens were cured for 28 days. After curing, the specimens were taken out of the curing tank and oven-dried at 50 °C for 24 h. All specimens were cooled to room temperature (for at least 24 hours) prior to testing.

3.3.2. Full-scale airport pavement slab

A 15×12 ft² (4.6×3.7 m²) concrete pavement slab (Fig. 2) was cast at the University of California Pavement Research Center (Davis, California) for HVS accelerated pavement testing (APT). Four 18×12×4 in³ (0.46×0.30×0.10 m³) self-sensing concrete regions (*i.e.*, B1, B2, B3, and B4) were cast along a longitudinal edge of the slab as shown in Fig. 2, while the remainder of the slab was normal concrete. The locations of B1 to B4 were selected according to where damage would most likely occur. The same mix design described in Section 3.1 was used.

Prior to casting, each self-sensing concrete regions was separated from its surrounding using a rectangular wooden mold of size 18×12×4 in³ (~ 450×300×100 mm³). Fishing wires were routed in the mold for facilitating electrode placement and for securing their position during casting. These wires were slightly displaced from the edges of the mold to provide room for normal and self-sensing concrete to mix during casting, similar to the procedure used when casting Type C specimens. As in Section 3.3.1, electrodes were prepared by cutting copper mesh to form 0.6×3 in² (15×75 mm²) rectangular strips. They were arranged in a 10×6 rectangular pattern and mounted onto fishing wires (Fig. 3). The electrodes were slightly shorter than the thickness of the pavement so that they could be completely embedded in concrete. Shielded multi-strand electrical wires (22 American Wire Gauge) were soldered to the bottom of the copper
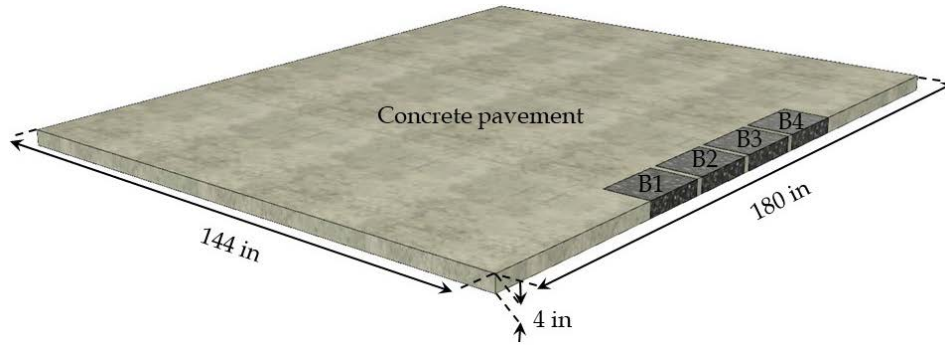
Figure 2. A 15×12 ft² (4.6×3.7 m²) concrete airport pavement slab was cast for accelerated pavement testing. B1, B2, B3, and B4 are the four self-sensing concrete regions located along one of the longitudinal edges of the slab.

mesh electrodes and then routed along the longitudinal end of the slab for connection with the ERT data acquisition (DAQ) system.

Two PMFLS-60 concrete strain gages (Tokyo Sokki Kenkyujo) were also installed at the center and in the longitudinal direction of each self-sensing concrete region, as shown in Fig. 4a. The top strain gage was placed at 1 in (~ 25 mm) below the top surface, while the bottom one was ~ 25 mm above the bottom of the slab. These reference strain gages were installed to measure the internal strain response of each self-sensing concrete region.

After the molds, electrodes, and strain gages were prepared, the entire concrete slab was cast. First, self-sensing concrete was mixed on-site with a 9 ft³ (0.25 m³) Multiquip mixer. The self-sensing concrete mix was poured into the wooden molds and consolidated with a poker vibrator. Second, and at the same time, plain concrete (Syar Concrete LLC.) was poured directly from a cement mixer truck in the remaining area and consolidated. Then, the wooden molds around the self-sensing concrete regions were removed, where the two different concrete mixes were allowed to naturally mix at the interface. The final step entailed smoothing the slab surface followed by spraying of a curing compound to minimize water evaporation and subsequent microcracks. A picture of the slab immediately after casting is shown in Fig. 4b. The concrete was cured for 28 days; Fig. 4c shows a picture of the cured slab.
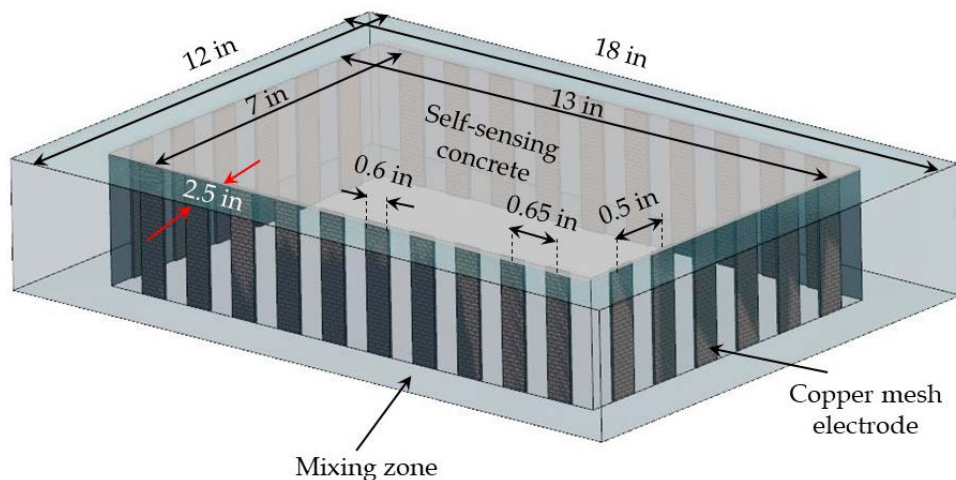


Figure 3. An illustration and the dimensions of the self-sensing concrete block casted as part of the full-scale airport pavement slab are shown. The electrodes were arranged in a 10×6 rectangular pattern in the wooden mold.

Figure 4. (a) The wooden mold for casting the self-sensing concrete regions, along with the electrodes mounted on fishing wires and strain gages, are shown. The picture of concrete slab (b) immediately after casting and (c) after 28 days of curing are shown.

### 3.4. Spatial Damage Detection Tests

### 3.4.1. Laboratory testing protocols

Spatial damage detection tests were performed by inflicting different types of damage and performing ERT on self-sensing concrete specimens. The ERT DAQ system was assembled by interfacing a Keithley 6221 current source with a Keysight 34980A multifunctional switch. The switch was controlled by a custom *Matlab* program to sequentially inject DC (on the order of mA) across any chosen pair of boundary electrodes, while the compliance voltage of the source was maintained at 105 V. During testing, the applied DC current was set to take advantage of the full voltage measurement range of the ERT DAQ system. Then, voltage differences between the remaining pairs of boundary electrodes were simultaneously recorded by the built-in digital multimeter (DMM) in the switch. An "across injection pattern" was used for all the experiments. It should be noted that the DC magnitude of the injected current was set to span the voltage measurement range of the DAQ to maximize SNR. Details about the DAQ system and the ERT excitation and measurement protocols can be found in Loyola *et al.* [42].

Prior to introducing damage to any of the specimens, a baseline ERT measurement was obtained. The first experiment was performed by drilling a hole at the center of a Type A specimen using a 0.25-in-diameter (~ 6.25 mm) masonry drill bit. The second experiment used an electric table saw to cut a thin groove on the specimen surface to simulate a crack. An additional orthogonal, crack-like cut was introduced thereafter. Due to this cutting method, cracks were deeper in the middle as compared to its ends. It should be mentioned that the grooves were cut on the backside of the specimen to prevent damaging the electrodes. Next, damage was introduced to Type B specimens by drilling multiple holes at different locations using a 1-in-diameter (~ 25 mm) masonry drill bit. The last set of experiments aimed to detect the severity of damage in a Type C specimen. A ~ 6.25 mm hole was drilled halfway through the specimen near its bottom-left corner to simulate minor damage. Damage severity was further increased by drilling through the remaining half of the thickness at the same spot. For all tests, ERT measurements were acquired after each new damage feature was introduced.

### 3.4.2. HVS APT

Accelerated pavement testing of the concrete airport pavement slab was performed using a heavy vehicle simulator. Similar to the laboratory experiments, baseline ERT measurements were recorded prior to applying any load to the slab. Baseline recorded at a particular time can be used to characterize the damage that occurred after that time. Hence, the effect of damage that occurred before the baseline measurements can be avoided from the final reconstructed images.

Then, the HVS applied bi-directional traffic using a dual wheel assembly traveling along the longitudinal direction. The outside edge of one of the two wheels aligned with the longitudinal edge of the

Table 2. The applied carriage load corresponding to different loading cycles are shown.

| Loading cycles | Carriage load |
|---|---|
| 0 to 1,000 | 25 kN |
| 1,001 to 6,000 | 40 kN |
| 6,001 to 9,000 | 60 kN |
| 9,001 to 15,000 | 80 kN |
| 15,001 to 17,000 | 100 kN |

slab during trafficking. As a result, one of the wheels passed right over the self-sensing concrete blocks during trafficking (Fig. 4c). The HVS was commanded to apply a total of 17,000 cycles of loading on the pavement, with the applied carriage load gradually increasing from 25 kN to 100 kN based on the schedule listed in Table 2. After every 1,000 cycles of loading, the HVS was paused, and ERT measurements of all four self-sensing concrete regions were acquired. The locations of surface cracks, if any, were also manually marked after every 1,000 cycles. It should be mentioned that the ERT measurements were recorded during sunny and dry weather so that the effect of moisture on the ERT results could be minimized.

## 4. Results and Discussion

### 4.1. Small-Scale Specimen ERT Test Results

First, as mentioned in Section 3.4.1, a 6.25-mm-diameter hole was drilled at the center of Type A specimens (Fig. 5a). The FEM for ERT conductivity reconstruction of Type A specimens used 400 bilinear quadrilateral elements. The hole was drilled through the specimen's thickness starting from its front-side (*i.e.*, the face with access to the electrodes). During drilling, minor spalling of concrete occurred on the backside near the drilled location, as is highlighted in Fig. 5b. Fig. 5c shows the corresponding ERT-estimated change in spatial conductivity distribution (with respect to the undamaged baseline), and a negative change in conductivity was observed at the center. This was expected since the drilled hole removed material, which reduced conductivity at the damaged region. The shifting of the predicted damage spot towards the left was due to spalling of self-sensing concrete at the backside of the specimen. Overall, the shape of the damage as indicated by the ERT conductivity map (Fig. 5c) closely resembled the actual shape of the damage shown in Fig. 5b. Low SNR observed in Fig. 5c was probably due to the lowest damage sensitivity of the central region of the ERT specimen caused by the diffusive nature of the injected current. In addition to validating the proposed system's damage detection capability, this result demonstrated its potential to identify a subsurface defect that was not visible from the front-side of the concrete specimen.

Another experiment was performed on Type A specimens to validate crack detection using ERT. The specimen was subjected to damage by cutting grooves along its diagonals (Figs. 6a and 6b). Their corresponding changes in spatial conductivity are shown in Figs. 6c and 6d, respectively. Similar to Fig. 5, a decrease in conductivity was observed along the region of the diagonal cuts. The shapes and orientation of the cuts were also successfully captured in the reconstructed conductivity maps. As mentioned in Section 3.4.1, the depth of the cut was not uniform along its length and was ~ 0.52 in (~ 13 mm) near the center and ~ 0.20 in (~ 5 mm) near the corners, with an average width was ~ 0.28 in (~ 4.5 mm). As a result, the magnitude of conductivity change (decrease) was greatest at the center and gradually lessened toward the ends of the diagonals. Despite identifying the location, shape, size, and severity of the cracks, blurriness in the reconstructed conductivity maps was observed. This could have resulted as the electrical current could not thoroughly propagate between two opposite electrodes due to the closely-spaced cracks [50]. The sharpness of the ERT images can be enhanced by increasing the number of boundary electrodes, thereby collecting more voltage measurements at the boundary.
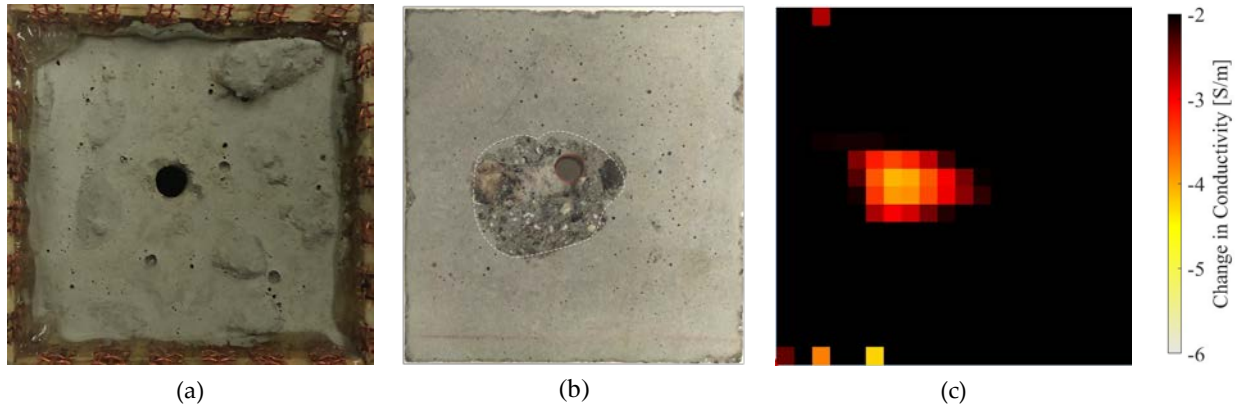
Figure 5. (a) Damage was introduced in an 80×80×18 mm³ Type A self-sensing concrete specimen by drilling a 6.25-mm-diamter hole near the center. (b) Spalling has occurred on the back-side of the concrete specimen. (c) The change in conductivity distribution with respect to its undamaged state was calculated using ERT.
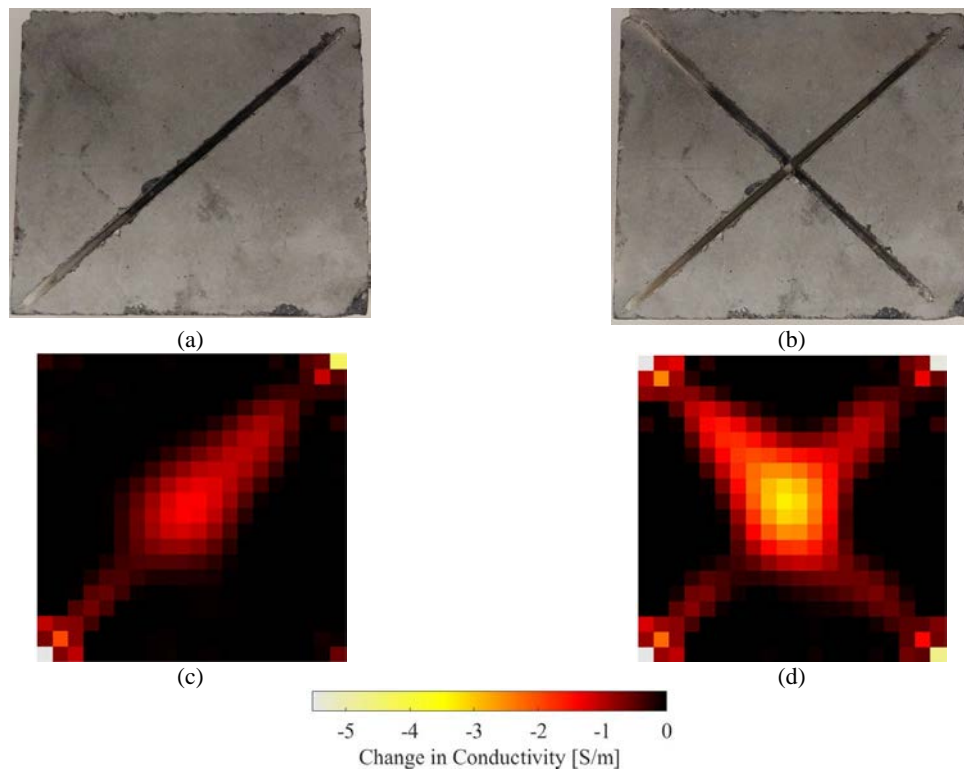


Figure 6. (a) A diagonal cut was made on the backside of a 80×80×18 mm³ Type A self-sensing concrete specimen to create the first damage state, (b) followed by another orthogonal cut to create the second damage state. The ERT results successfully characterized the (c) single and (d) double diagonal cuts.

Second, holes were drilled near the bottom-left and top-left corners of Type B specimens, while ERT datasets were acquired after each new damage state. The FEM for ERT conductivity reconstruction of Type B specimens used 289 bilinear quadrilateral elements. Figs. 7a and 7b show pictures of the same specimen after each hole was drilled. The corresponding changes in conductivity obtained by solving the ERT inverse algorithm are presented in Figs. 7c and 7d, respectively. Like the previous cases, ERT successfully identified the sizes and locations of these damage features. Significant decreases in electrical conductivity at the locations of drilled holes were observed due to the severity of damage (*i.e.*, through-holes). In principle, these through-holes have zero conductivity or an infinite change in resistivity with respect to the pristine state. However, infinite resistivity cannot be mathematically represented nor could an extremely
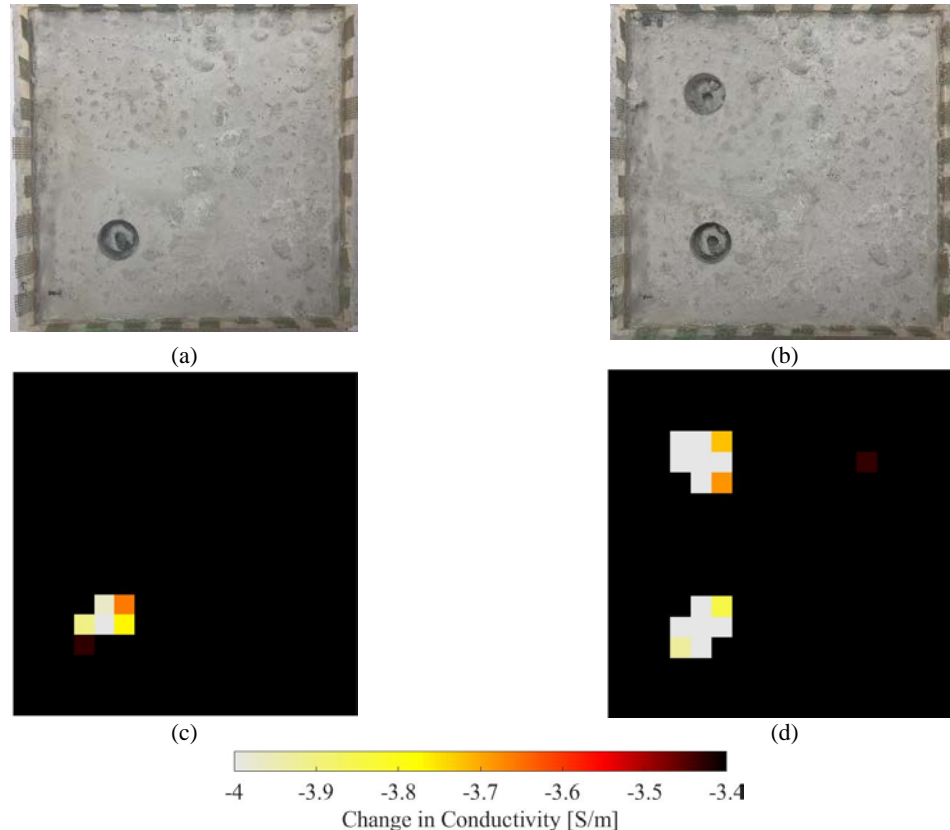
Figure 7. Two 25-mm-diamter holes were drilled at the (a) bottom-left and (b) top-left corner of the Type B specimen. The corresponding changes in conductivity are shown in (c) and (d) respectively.

large value be estimated by ERT due to regularization. Nevertheless, these results demonstrate that ERT can be implemented on self-sensing concrete specimens as large as $1\times1$ ft$^2$.

The last laboratory experiment was performed using a Type C specimen, and the purpose was to validate detection of progressive damage. First, a hole was drilled at the bottom-left corner of the specimen to only half the specimen thickness (*i.e.*, ~ 25-mm-deep). The FEM for ERT conductivity reconstruction of Type C specimens used 1,092 bilinear quadrilateral elements. The corresponding ERT result is shown in Fig. 8a. Next, hole depth was extended by drilling through the entire thickness. ERT measurements were again acquired for conductivity reconstruction. The ERT conductivity map of Fig. 8b not only correctly showed the location of the damage but also an appropriate greater change in conductivity. This result was expected since conductivity changes would be greater with increasing damage severity. Overall, the results of Fig. 8 validate that ERT could characterize progressive damage in larger self-sensing concrete specimens.

Although the experimental results presented in this section validated spatial damage detection, the damage sizes as determined by ERT were slightly overestimated in all cases. This overestimation can be attributed to the inherent resolution issue of the inverse problem, which is limited by the number of boundary current excitations and voltage measurements, as well as the large spacing between electrodes. To overcome this issue, more electrodes can be instrumented to obtain more independent measurements for solving the ERT inverse problem. In addition, the regularization scheme used may have also blurred the reconstructed images. Further improvements can be made by imposing a total variation (TV) regularization scheme with an iterative algorithm [36, 58] . Nevertheless, these results confirmed that ERT can be used to characterize different types of spatially distributed damage in self-sensing concrete.
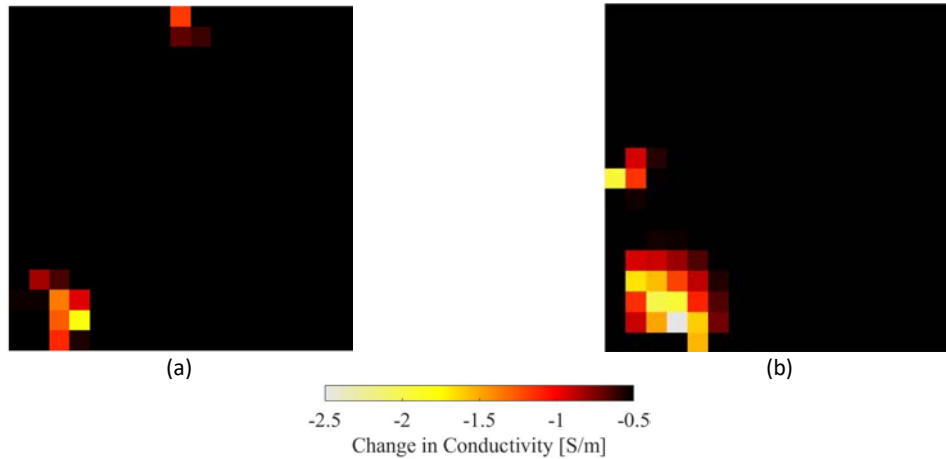
Figure 8. (a) A partial hole was drilled at the bottom-left corner of a Type C specimen, and its corresponding change in conductivity distribution relative to its undamaged state is shown. (b) The hole was then completely drilled through the thickness, and the ERT result shows a greater change (decrease) in conductivity where the hole was drilled.

### 4.2. HVS APT ERT Results

As mentioned in Section 3.2, HVS accelerated pavement tests were conducted on a full-scale concrete airport pavement slab with four embedded self-sensing concrete regions. A final picture of the damaged pavement slab after 17,000 cycles of loading is shown in Fig. 9. The locations of the self-sensing concrete regions B1 to B4 are also outlined. Cracks were also manually marked on the slab after every 1,000 cycles of loading (Fig. 9), during which ERT tests were also performed. The number of cycles after when these cracks appeared are also indicated in Fig. 9.

Fig. 10 presents the reconstructed change in electrical conductivity distributions of self-sensing concrete region B1 after every 1,000 loading cycles of HVS APT. The number at the top left corner of each image corresponds to the number of cycles applied. A negative change in conductivity was observed near the top-right corner of B1 early in the tests, and it remained approximately the same size and magnitude as
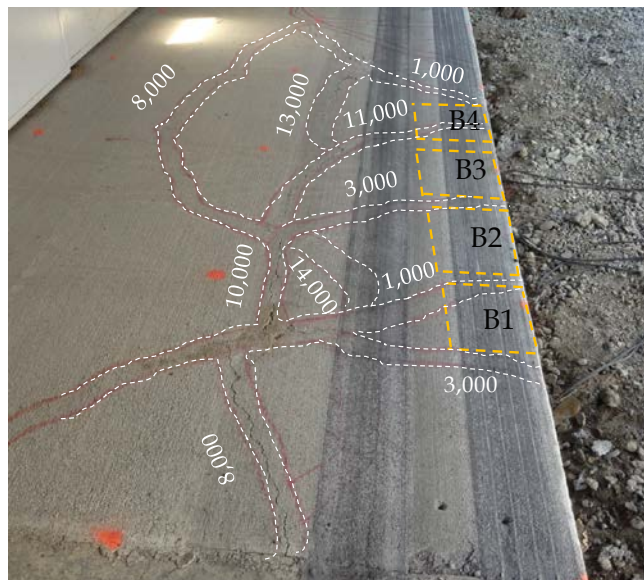


Figure 9. The picture of the damaged concrete pavement slab after 17,000 cycles of HVS testing shows the locations of the four self-sensing concrete regions. Cracks were marked at the end of each 1,000-cycle period as they appeared.
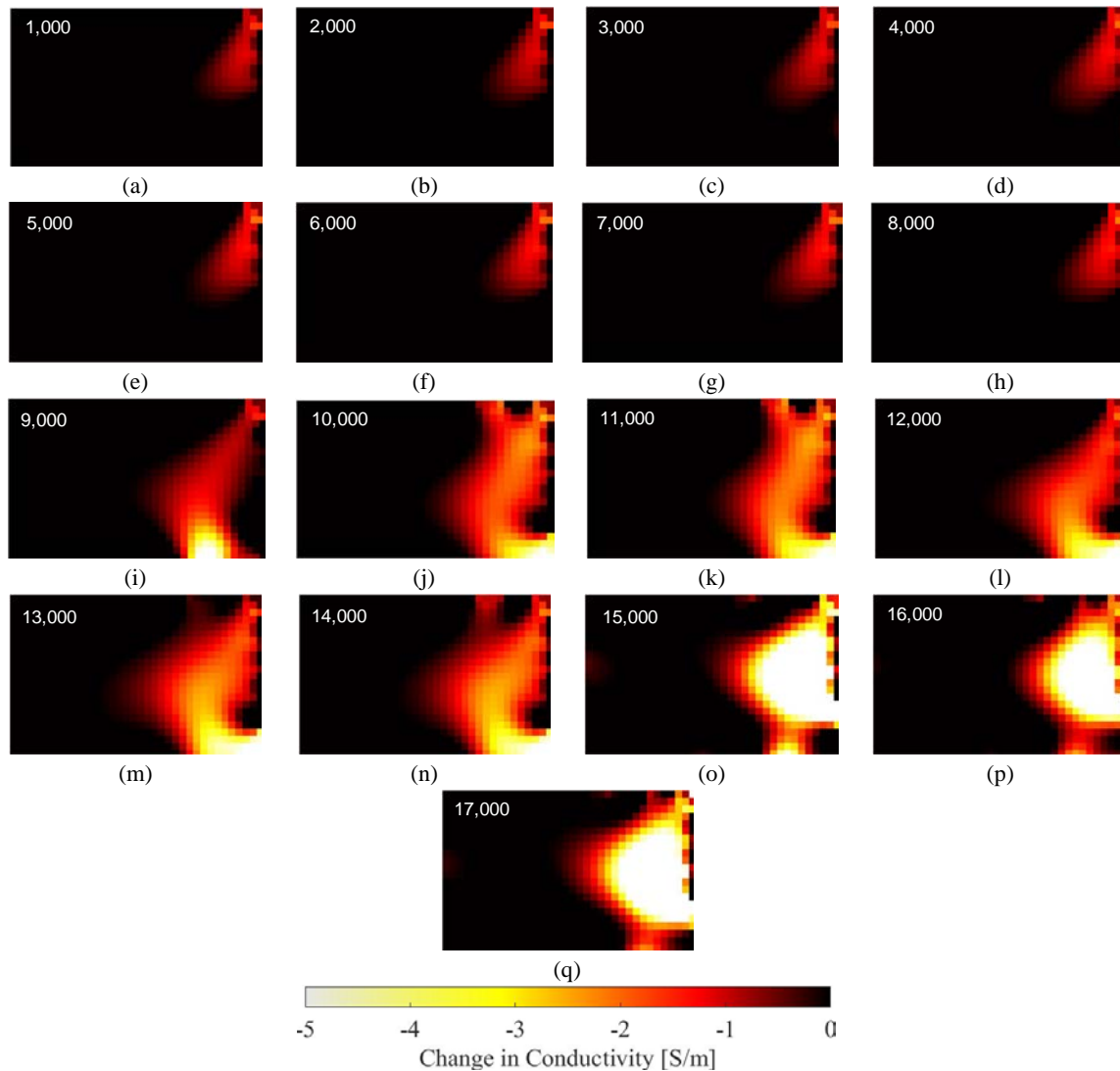
Figure 10. (a) to (q) The ERT results show the change in conductivity distribution (with respect to its undamaged baseline) of self-sensing concrete region B1 after the HVS testing to different loading cycles (as highlighted in each image).

shown in Figs. 10a to 10h. This location coincides with the first crack that appeared after 1,000 cycles of loading, as is also marked in Fig. 9. The similarity of the conductivity maps in Figs. 10a to 10h suggests that this crack did not propagate significantly during the first 8,000 cycles of loading.

However, further decreases in conductivity at the damaged location was captured by ERT with additional loading cycles, as are shown in Figs. 10i to 10q. As mentioned in Table 2, the load was increased to 80 kN after 9,000 cycles. It can be inferred that the crack propagated and widened from 8,000 to 17,000 cycles due to fatigue and the higher intensity of loads applied, which resulted in more significant changes in electrical conductivity in that region. Unfortunately, ERT was unable to capture the final shape of the crack marked on the surface of B1 (Fig. 9). Rather, an intense change in conductivity was observed near the right edge. This phenomenon can be potentially attributed to the presence of another severe subsurface crack near this region (as suggested by the ERT results from Figs. 10o to 10q) that masked the surface crack observed in Fig. 9.
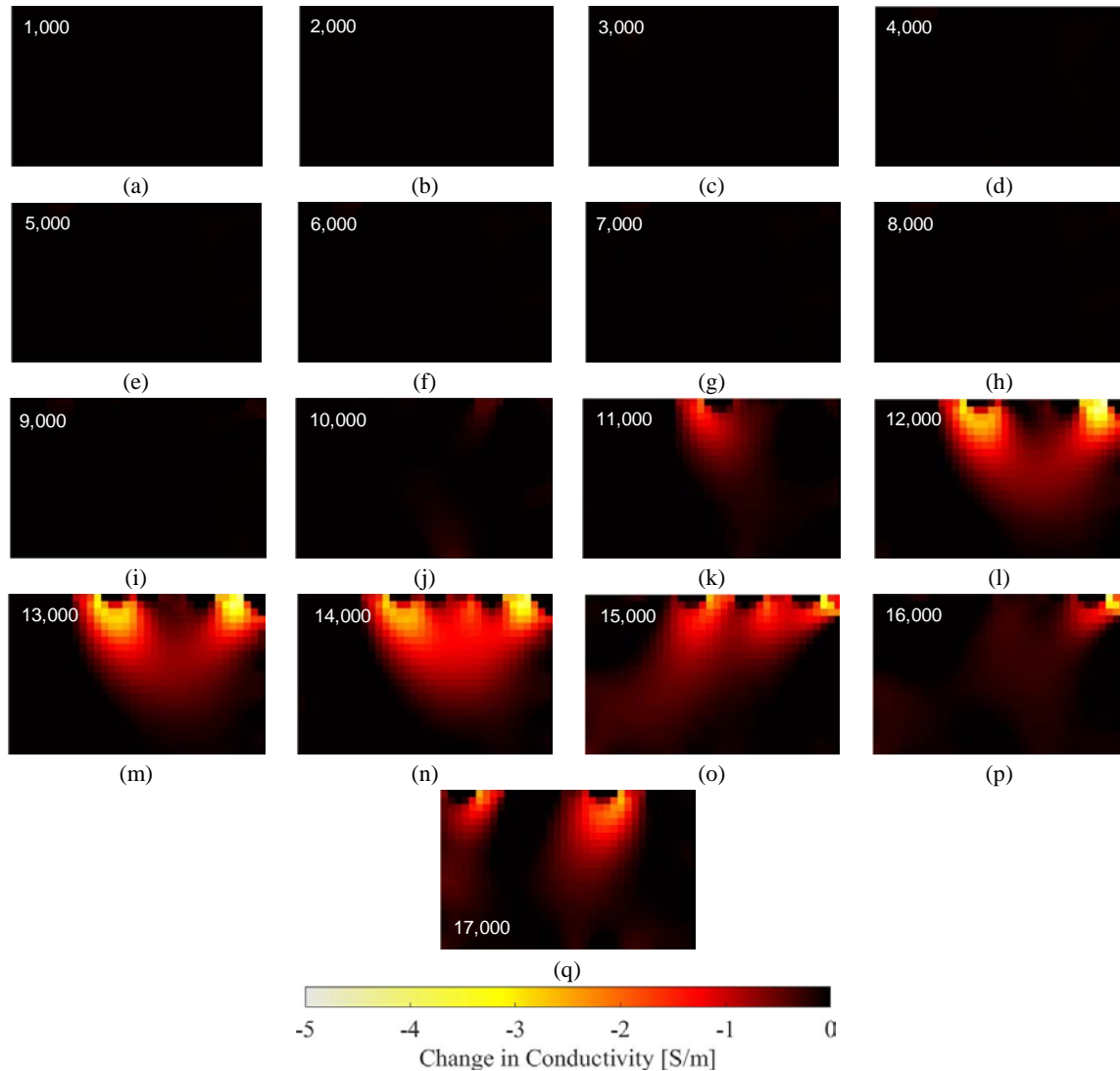
Figure 11. (a) to (q) These ERT results present the conductivity changes experienced by B2 at after different cycles of loading.

Although no surface cracks passed through B2 and B3 (Fig. 9), some conductivity changes were recorded in these regions, as shown in Figs. 11 and 12. However, the locations of these conductivity changes were slightly inconsistent between consecutive loading stages. It was also observed that the magnitude of the conductivity changes shown in Figs. 11 and 12 were much lower than those in Fig. 10. Such low-magnitude conductivity changes could occur due to measurement noise.

Fig. 13 shows a picture of self-sensing concrete region B4 after 11,000 cycles of loading, where a crack appeared and then traversed through the middle of its bottom edge. Fig. 14 shows the changes in conductivity distribution of B4 corresponding to different loading stages from 1,000 to 17,000 cycles. From 1,000 to 4,000 cycles, a minor change in conductivity was observed near the middle of the bottom edge (Figs. 14a to 14d), yet no damage was observed on the surface. Continued loading from 5,000 to 10,000 cycles still revealed no damage on the surface, but the ERT results showed a continued progression of greater conductivity changes (Figs. 14e to 14j). This localized conductivity change was potentially the result of a subsurface crack that formed at ~ 3,000 cycles and had slowly but not yet fully propagated to the surface until it was visually identifiable at 10,000 cycles.
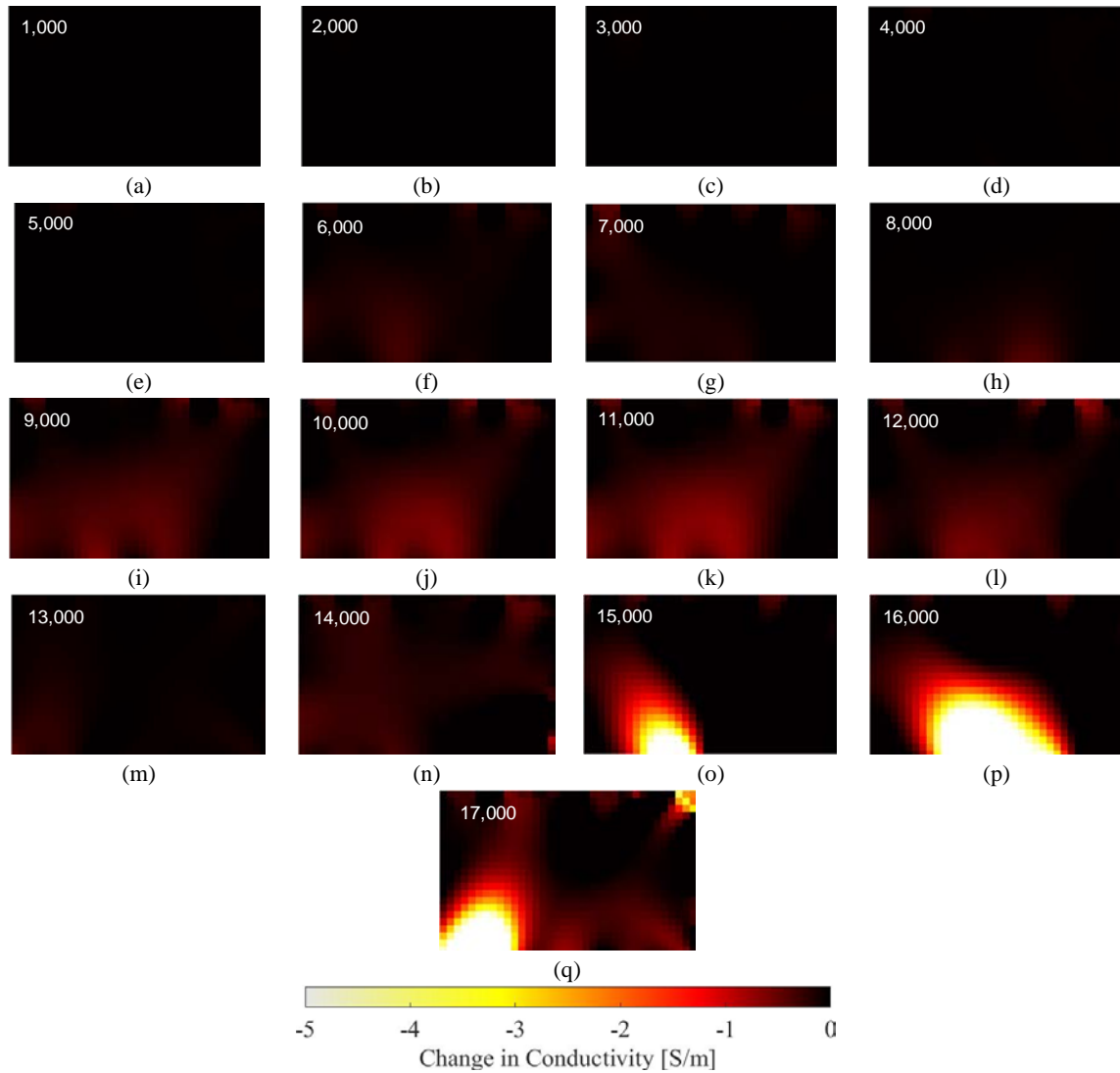
Figure 12. (a) to (q) The ERT results present the conductivity changes experienced by B3 after different stages of loading.



Figure 13. A zoomed-in view of B4 after 11,000 cycles of loading. The observed crack location is highlighted in red.

It can be seen from Fig. 9 that a surface crack appeared after 11,000 loading cycles in the middle of the bottom edge of B4. The location of the crack coincided with the conductivity changes shown in the corresponding ERT conductivity maps (Fig. 14k). In fact, the crack appeared immediately after significant
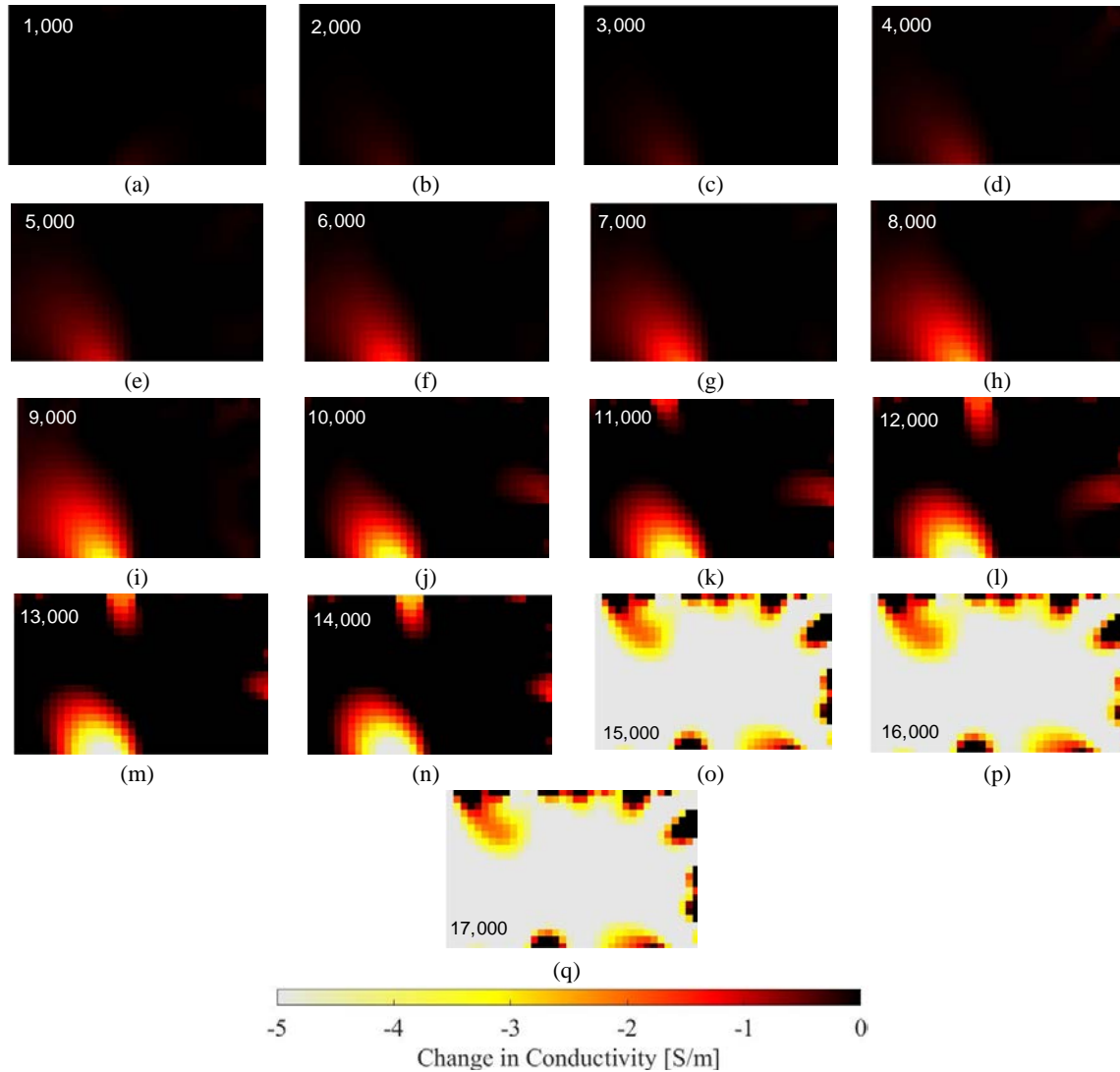
Figure 14. The ERT results of B4 corresponding to different loading stages are shown.

conductivity changes were captured by ERT (Figs. 14c to 14j). In addition, closer inspection of Fig. 14k revealed that the shape of the conductivity change resembled the crack propagation path. This result is significant, because it directly indicates that ERT was able to track and localize subsurface defects prior to them appearing (*e.g.*, even before 7,000 cycles of loading). Early detection of subsurface damage features allows airport owners and stakeholders to take necessary repair actions prior to damage propagating to become severe.

In all the results described above (*i.e.*, Figs. 10, 11, 12, and 14), amplified conductivity changes near the boundaries were observed, especially during high intensity loading. For example, instead of capturing the observed crack's correct shape and path, the ERT results shown in Fig. 10 indicated an intensified change in conductivity near the right edge (Figs. 10i to 10q). In Figs. 11 and 12, some conductivity changes were observed only near the electrodes, although no such defects were observed on the concrete surface. In the case of B4, from 15,000 to 17,000 cycles, ERT failed to produce any meaningful results (Figs. 14o to 14q). It is possible that all such conductivity changes were observed due to the failure of certain electrodes inside the self-sensing concrete regions, thus producing spurious voltage measurements and inaccurate reconstructed conductivity maps. This hypothesis warrants future testing explicitly focusing on the

electrode-concrete interface. If electrodes did in fact disbond from the self-sensing concrete, using a lower-density-grid copper mesh could help the concrete mix flow in between mesh grids and form a stronger physical connection to these electrodes.

It should be mentioned that excessive moisture inflow in the concrete could exaggerate the accuracy of the difference imaging algorithm (*e.g.*, NOSER algorithm used in this study) [59]. Such moisture ingress creates background inhomogeneity that could violate the underlying homogeneous background assumption of the difference imaging algorithm [50]. However, an inference can be drawn such that there was negligible moisture ingress since ERT measurements were recorded during sunny and dry weather. In addition, it could be possible that incorporation of MWCNT thin film at the cement-aggregate interfaces facilitated electrical current conduction to create uniform electrical conductivity throughout the concrete blocks, which made them more resistant to slight fluctuations in moisture content. As the change in conductivity of the self-sensing concrete due to damage was more prominent than the effects of moisture, the NOSER algorithm was able to capture the damage-induced conductivity changes. Effects of moisture will be investigated in future studies.

Although nominal steel reinforcement is required in concrete pavement [4], no reinforcement was used in this study. The presence of the highly conductive steel reinforcements in the concrete could alter the electrical current propagation that could affect ERT's damage sensing performance. That said, the locations and the conductivity of the reinforcements can be incorporated as part of the ERT forward model. In doing so, the influence of the steel reinforcement on current propagation can be precisely modeled, and its effect on conductivity reconstruction can be avoided.

Overall, this full-scale experiment successfully validated that self-sensing concrete, coupled with ERT, could be implemented to identify spatially distributed damage (such as cracks) in concrete airport pavements so long as a good connection between the concrete and the electrodes is ensured. As compared to visual inspection, ERT offers the added benefit of mapping cracks and the ability to detect and characterize damage precursors such as subsurface cracks.

## 5. Conclusions

The objective of this study was to validate that self-sensing concrete and an electrical resistance tomography measurement strategy and algorithm could be used for mapping damage in full-scale concrete airport pavements. First, self-sensing concrete was fabricated using fine and coarse aggregates pre-coated with MWCNT-latex thin films. Second, small-scale concrete specimens were cast, and they were instrumented with sets of boundary electrodes for ERT testing. Artificial damage in the form of drilled holes and cuts were introduced, and the reconstructed electrical conductivity distributions of these self-sensing concrete specimens successfully validated ERT for detecting the locations, shapes, and severities of the introduced damage features. Last, a full-scale airport concrete pavement slab with four self-sensing concrete regions was cast. APT was conducted, where an HVS applied 17,000 cycles of gradually increasing loads (25 kN to 100 kN) to induce damage. ERT measurements were collected after every 1,000 cycles of loads. As localized damage altered the electrical conductivity of the self-sensing concrete regions, the reconstructed ERT conductivity maps were able to reveal the shapes, severities, and locations of these internal damage features so long as the bonding between the electrodes and concrete was intact. Even subsurface damage that was not visible at the surface was successfully identified by ERT. The locations of these cracks were verified once some of these cracks have propagated to the surface and were visually identified. Future studies will investigate the long-term sensing and mechanical behavior of self-sensing concrete subjected to complex and even more realistic loading scenarios.

## Acknowledgments

## References

1. Loh KJ, and Gonzalez J. Cementitious Composites Engineered with Embedded Carbon Nanotube Thin Films for Enhanced Sensing Performance. Journal of Physics: Conference Series. 2015; 628(1): 012042.
2. Gonzalez JG, Gupta S, and Loh KJ. Multifunctional Cement Composites Enhanced with Carbon Nanotube Thin Film Interfaces. Proceedings of the IEEE. 2016; 104(8): 1547-1560.
3. Gupta S, Gonzalez JG, and Loh KJ. Self-Sensing Concrete Enabled by Nano-Engineered Cement-Aggregate Interfaces. Structural Health Monitoring. 2017; 16(3): 309-323.
4. Kim J, and Hjelmstad KD. Three-Dimensional Finite Element Analysis of Doweled Joints for Airport Pavements. Transportation Research Record. 2003; 1853(1): 100-109.
5. White G. Limitations and Potential Improvement of The Aircraft Pavement Strength Rating System to Protect Airport Asphalt Surfaces. International Journal of Pavement Engineering. 2017; 18(12): 1111-1121.
6. Mullen M "Special Inspections of Paved Areas During Excessive Heat Periods," Central Region Airport Certification Bulletin, Federal Aviation Administration, Central Region, Airports Division, Kansas City, MO (2001).
7. Cheng HD, Chen JR, Glazier C, and Hu YG. Novel Approach to Pavement Cracking Detection based on Fuzzy Set Theory. Journal of Computing in Civil Engineering. 1999; 13(4): 270-280.
8. Kong X, and Li J. Vision-based Fatigue Crack Detection of Steel Structures using Video Feature Tracking. Computer-Aided Civil and Infrastructure Engineering. 20018; 33(9): 783-799.
9. Gopalakrishnan K, Khaitan SK, Choudhary A, and Agrawal A. Deep Convolutional Neural Networks with Transfer Learning for Computer Vision-based Data-driven Pavement Distress Detection. Construction and Building Materials. 2017; 357 322-330.
10. Radopoulou SC, and Brilakis I. Patch Detection for Pavement Assessment. Automation in Construction. 2015; 53 95-104.
11. Koch C, Georgieva K, Kasireddy V, Akinci B, and Fieguth P. A review on Computer Vision Based Defect Detection and Condition Assessment of Concrete and Asphalt Civil Infrastructure. Advanced Engineering Informatics. 2015; 29(2): 196-210.
12. Zhao H, Wu C, Wang X, and Zheng Y. Pavement Condition Monitoring System at Shanghai Pudong International Airport. Pavement Materials, Structures, and Performance. 2014; 283-295.
13. Shukla A, Jain N, and Chona R. A Review of Dynamic Fracture Studies in Functionally Graded Materials. Strain. 2007; 43 76-95.
14. Henschen JD, Amirkhanian AN, Roesler JR, and Lange DA. Field Evaluation of Alternate Isolation Joints at O'Hare International Airport, Conf Proc 2014 FAA Worldwide Airport Technology Transfer Conference. 2014.
15. Zhou Z, Liu W, Huang Y, Wang H, Jianping H, Huang M, Jingping O, and (2012), , No. 28, pp. 36-49. Optical Fiber Bragg Grating Sensor Assembly for 3d Strain Monitoring and Its Case Study in Highway Pavement. Mechanical Systems and Signal Processing. 2012; 28 36-49.
16. Kahandawa GC, Epaarachchi J, Wang H, and Lau KT. Use of FBG Sensors for SHM in Aerospace Structures. Photonic Sensors. 2012; 2(3): 203-214.
17. Deng YS, and Sun BJ. Researches on Intelligent Material System and its Application to Civil Engineering. Architecture Technology. 2005; 36(2): 92-95.
18. Hugenschmidt J, Partl MN, and Witte HD. GPR Inspection of A Mountain Motorway in Switzerland. Journal of Applied Geophysics. 1998; 40(1-3): 95-104.
19. Moropoulou A, Avdelidis NP, Koui M, and Kakaras K. An Application of Thermography for Detection of Delaminations in Airport Pavements. NDT & E International. 2001; 34(5): 329-335.
20. Maser KR, and Roddis WK. Principles of Thermography and Radar for Bridge Deck Assessment. Journal of Transportation Engineering. 1990; 116(5): 583-601.
21. Lin VW, Li M, Lynch JP, and Li VC. Mechanical and Electrical Characterization of Self-Sensing Carbon Black ECC, Conf Proc Nondestructive Characterization for Composite Materials, Aerospace Engineering, Civil Infrastructure, and Homeland Security. 2011; 798316.
22. Wong I, Loh KJ, Wu R, and Garg N. Sensing Properties of Mortar Incorporating Ultra-Low Concentrations of Carbon-based Conductive Additives, Conf Proc 5th Asia-Pacific Workshop on Structural Health Monitoring Conference. 2014.
23. Han BG, Yu Y, Han BZ, and Ou JP. Development of a Wireless Stress/Strain Measurement System Integrated with Pressure-Sensitive Nickel Powder-Filled Cement-Based Sensors. Sensors and Actuators A: Physical. 2008; 147(2): 536-543.
24. Khoury S, Aliabdo AA, and Ghazy A. Reliability of Core Test–Critical Assessment and Proposed New Approach. Alexandria Engineering Journal. 2014; 53(1): 168-184.
25. Meyyappan M. Carbon Nanotubes: Science and Applications. NASA Ames Research Center, Moffett Field, CA:CRC Press;2004.
26. Tombler TW, Zhou C, Alexseyev L, Kong J, Dai H, Liu L, Jayanthi CS, Tang M, and Wu SY. Reversible Electromechanical Characteristics of Carbon Nanotubes Underlocal-Probe Manipulation. Nature. 2000; 405(6788): 769.
27. Li GY, Wang PM, and Zhao X. Pressure-Sensitive Properties and Microstructure of Carbon Nanotube Reinforced Cement Composites. Cement and Concrete Composites. 2007; 29(5): 377-382.
28. Yu X, and Kwon E. A carbon nanotube/cement composite with piezoresistive properties. Smart Materials and Structures. 2009; 18(5): 055010.
29. Han B, Yu X, and Kwon E. A Self-Sensing Carbon Nanotube/Cement Composite for Traffic Monitoring. Nanotechnology. 2009; 20(44): 445501.
30. Chung DD. Dispersion of Short Fibers in Cement. Journal of Materials in Civil Engineering. 2005; 17(4): 379-383.
31. H.Wang, Gao X, and Wang R. The Influence of Rheological Parameters of Cement Paste on the Dispersion of Carbon Nanofibers and Self-sensing Performance. onstruction and Building Materials. 134 673-683.

32.	Ferrara L, and Meda A. Relationships Between Fibre Distribution, Workability and the Mechanical Properties of SFRC Applied to Precast Roof Elements. Materials and Structures. 2006; 39(4): 411-420.

33.	Mechtcherine V, Michel A, Liebscher M, Schneider K, and Großmann C. Mineral-impregnated Carbon Fiber Composites as Novel Reinforcement for Concrete Construction: Material and Automation Perspectives. Automation in Construction. 2020; 110 103002.

34.	Loh KJ and Gonzalez JG. Multifunctional Cement Composites with Load-Bearing and Self-Sensing Properties. U.S. Patent 2016/0340245 A1. Issued November 24, 2016.

35.	Gupta S, Gonzalez J, and Loh KJ. Damage Detection using Smart Concrete Engineered with Nanocomposite Cement-Aggregate Interfaces, Conf Proc 10th International Workshop on Structural Health Monitoring. 2015.

36.	Soleimani M. Image and Shape Reconstruction Methods in Magnetic Induction and Electrical Impedance Tomography. Ph.D. Department of Mathematics. University of Manchester. Manchester, England. 2005.

37.	Yerworth RJ, Bayford RH, Brown B, Milnes P, Conway M, and Holder DS. Electrical Impedance Tomography Spectroscopy (EITS) for Human Head Imaging. Physiological Measurement. 2003; 24(2): 477-489.

38.	Adler A, Amyot R, Guardo R, Bates JH, and Berthiaume Y. Monitoring Changes in Lung Air and Liquid Volumes with Electrical Impedance Tomography. Journal of Applied Physiology. 1992; 83(5): 1762-1767.

39.	Sarker SA, Mahalanabis D, Bardhan PK, Alam NH, Rabbani KS, Kiber A, Hassan M, Islam S, Fuchs GJ, and Gyr K. Noninvasive Assessment of Gastric Acid Secretion in Man (Application of Electrical Impedance Tomography (EIT)). Digestive Diseases and Sciences. 1997; 42(8): 1804-1809.

40.	Jeong WC, Meng ZJ, Kim HJ, Kwon OI, and Woo EJ. Experimental Validations of In Vivo Human Musculoskeletal Tissue Conductivity Images using MR-Based Electrical Impedance Tomography. Bioelectromagnetics. 2014; 35(5): 363-372.

41.	Hou TC, Loh KJ, and Lynch JP. Spatial Conductivity Mapping of Carbon Nanotube Composite Thin Films by Electrical Impedance Tomography for Sensing Applications. Nanotechnology. 2007; 18(31): 315501.

42.	Loyola BR, Saponara VL, Loh KJ, Briggs TM, O'Bryan G, and Skinner JL. Spatial Sensing using Electrical Impedance Tomography. IEEE Sensors Journal. 2013; 13(6): 2357-2367.

43.	Hou TC, and Lynch JP. Electrical Impedance Tomographic Methods for Sensing Strain Fields and Crack Damage in Cementitious Structures. Journal of Intelligent Material Systems and Structures. 2009; 20(11): 1363-1379.

44.	Hallaji M, Seppänen A, and Pour-Ghaz M. Electrical Impedance Tomography-Based Sensing Skin for Quantitative Imaging of Damage in Concrete. Smart Materials and Structures. 2014; 23(8): 085001.

45.	Seppänen A, Hallaji M, and Pour-Ghaz M. A Functionally Layered Sensing Skin for the Detection of Corrosive Elements and Cracking. Structural Health Monitoring. 2017; 16(2): 215-224.

46.	Tallman T, Gungor S, Wang K, and Bakis CE. Damage Detection and Conductivity Evolution in Carbon Nanofiber Epoxy via Electrical Impedance Tomography. Smart Materials and Structures. 2014; 23(4): 045034.

47.	Smyl D. Electrical Tomography for Characterizing Transport Properties in Cement-based Materials: A Review. Construction and Building Materials. 2020; 244 118299.

48.	Hallaji M, Seppänen A, and Pour-Ghaz M. Electrical Resistance Tomography to Monitor Unsaturated Moisture Flow in Cementitious Materials. Cement and Concrete Research. 2015; 69 10-18.

49.	Suryanto B, Saraireh D, Kim J, McCarter WJ, Starrs G, and Taha HM. Imaging water ingress into concrete using electrical resistance tomography. International Journal of Advances in Engineering Sciences and Applied Mathematics. 2017; 9(2): 109-118.

50.	Smyl D, Hallaji M, Seppänen A, and Pour-Ghaz M. Quantitative Electrical Imaging of Three-Dimensional Moisture Flow in Cement-based Materials. International Journal of Heat and Mass Transfer. 2016; 103 1348-1358.

51.	Liu T, Huang Y, Zou D, Teng J, and Li B. Exploratory Study on Water Seepage Monitoring of Concrete Structures using Piezoceramic Based Smart Aggregates. Smart Materials and Structures. 2013; 22(6): 065002.

52.	Vauhkonen M. Electric Resistance Tomography and Prior Information. Ph.D. Department of Mathematics. University of Kuopio. Kuopio, Finland. 1997.

53.	Yorkey TJ, Webster JG, and Tompkins WJ. Comparing Reconstruction Algorithms for Electrical Impedance Tomography. IEEE Transactions on Biomedical Engineering. 1987; BME-34(11): 843-852.

54.	Gupta S, Kim HE, Kim H, and Loh KJ. Planar Capacitive Imaging for Composite Delamination Damage Characterization. Measurement Science and Technology. 2020; 32(2): 024010.

55.	Hansen PC, and O'Leary DP. The Use of the L-curve in the Regularization of Discrete Ill-posed Problems. SIAM Journal on Scientific Computing. 1993; 14(6): 1487-1503.

56.	Zhang J, Leung CKY, and Cheung YN. Flexural Performance of Layered ECC-Concrete Composite Beam. Composites Science and Technology. 2006; 66(11-12): 1501-1512.

57.	Mortensen P, Ryu D, Zhao Y, and Loh KJ. Rapid Assembly of Multifunctional Thin Film Sensors for Wind Turbine Blade Monitoring. Key Engineering Materials Journal. 2013; 569 515-522.

58.	Gupta S, Lee HJ, Loh KJ, Todd MD, Reed J, and Barnett AD. Noncontact Strain Monitoring of Osseointegrated Prostheses. Sensors. 2018; 18(9): 3015.

59.	Smyl D, Hallaji M, Seppänen A, and Pour-Ghaz M. Three-dimensional Electrical Imaging of Moisture Ingress in Mortar. ACI Special Publication. 2016; SP-312—03 525.